Solar-Terrestrial Physics. 2024. Vol. 10. Iss. 3. P. 3–10. DOI: 10.12737/stp-103202401. © 2024
A.T. Altyntsev, M.V. Globa, N.S. Meshalkina, R.A. Sych. Published by INFRA-M Academic Publishing House

UDC 523.9-7, 523.98
DOI: 10.12737/stp-103202401

Received April 02, 2024
Accepted May 23, 2024

OBSERVATIONS OF CORONAL HOLES WITH THE SIBERIAN RADIOHELIOGRAPH

A.T. Altyntsev
Institute of Solar-Terrestrial Physics SB RAS, Irkutsk, Russia, altyntsev@iszf.irk.ru

M.V. Globa
Institute of Solar-Terrestrial Physics SB RAS, Irkutsk, Russia, globa@iszf.irk.ru

N.S. Meshalkina
Institute of Solar-Terrestrial Physics SB RAS, Irkutsk, Russia, nata@iszf.irk.ru

R.A. Sych
Institute of Solar-Terrestrial Physics SB RAS, Irkutsk, Russia, sych@iszf.irk.ru

Abstract. Multi-wavelength observations of a coronal hole (CH) with two-dimensional spatial resolution have been made for the first time in the frequency range from 2.8 to 12 GHz. At frequencies below 6 GHz, the average brightness of the hole is 1.5 times lower than the brightness level of the quiet Sun. The distribution of radio brightness over the hole is inhomogeneous: the ratio of maximum to minimum brightness temperatures falls from several times at low frequencies to tenths of fractions at the upper received frequencies. At frequencies above 6 GHz, the temperature contrast between the CH and regions of the quiet Sun is small. Within the CH, there are compact sources that are bright relative to the quiet Sun. In general, observations of CHs with SRH are promising both for the research into the nature of CHs and for the applied problems of forecasting solar wind characteristics.

Keywords: Sun, radio emission, bremsstrahlung, coronal holes.

INTRODUCTION

Coronal holes (CHs) are regions of reduced brightness in solar disk images in extreme ultraviolet (EUV) or soft X-ray emissions corresponding to configurations with open magnetic field lines [Cranmer, 2009]. CHs are sources of high-speed solar wind streams [Krieger et al., 1973; Nolte et al., 1976]. Data on their area and depth of brightness depression is used in forecasts of solar wind parameters in the vicinity of Earth [Vršnak et al., 2007; Obridko et al., 2009; Rotter et al., 2012, 2015; Reiss et al., 2016]. Emission depression is caused by the temperature and plasma density decreased relative to the quiet Sun in the transition region and contrasts most sharply in the 193 and 211 Å lines [Garton et al., 2018].

In the lower corona, CHs can manifest themselves as regions of depression of the brightness temperature of microwave radiation. The first CH radio spectra were obtained by large radio telescopes with beamwidths of several arcmin [Papagiannis, Baker, 1982]. It is shown that the highest contrast, up to 0.5 relative to the brightness temperature of the quiet Sun T_{QS}, is achieved at 0.6–0.75 GHz. In the microwave range, the contrast decreases and a depression of ~$0.8T_{QS}$ is observed at 3 GHz. Later, one-dimensional CH observations with an angular resolution of ~1′ were performed with the large radio telescope RATAN-600 in a wide frequency range from 1 to 15 GHz [Borovik et al., 1990; Dravskikh, Dravskikh, 2023]. A brightness temperature depression was observed at frequencies below 6–7 GHz. Spectral analysis showed that the depression was mainly caused by a halving of the plasma density in the corona over CH at heights up to $40 \cdot 10^3$ km. The plasma temperature in the corona over CHs can decrease by 20 %.

At frequencies above 10 GHz, where the corona's contribution to CH emission is small, the contrast with the surrounding regions of the quiet Sun is almost imperceptible.

Regular two-dimensional observations of CHs in microwaves with a spatial resolution to 10–20″ began in the 1990s at frequencies of 5.7 GHz (SSRT, [Grechnev et al., 2003]) and 17 GHz [Nakajima et al., 1994]. At 5.7 GHz, there was generally a brightness temperature depression in CHs to $8 \cdot 10^3$ K with a brightness temperature of the quiet Sun $16 \cdot 10^3$ K. The brightness temperature depression regions at 5.7 GHz were only in some cases close in shape to the CH visible in EUV emission [Krissinel et al., 2000]. In many cases, there were compact bright sources with temperatures to $22 \cdot 10^3$ K inside CHs. At 17 GHz, the contrast between CH and the quiet Sun is imperceptible, but in many cases sources of increased radio brightness were seen inside and on CH boundaries [Kosugi et al., 1986; Gopalswamy et al., 1999; Pohjolainen et al., 2000; Moran et al., 2001]. Various reasons for the appearance of such inhomogeneities at 17 GHz have been discussed: 1) microflares in the chromospheric network leading to energy release at CH bases [Gopalswamy et al., 1999]; 2) concentration of open magnetic field lines in the chromosphere, which correspond to their increased divergence in the corona [Wang, Sheely, 1990].

Characteristics of the microwave sources located inside CHs at frequencies with a small (17 GHz) and large (5.7 GHz) contribution of emission at coronal heights have been compared in [Maksimov et al., 2006]. It has been found that small-scale inhomogeneities at these frequencies are radially spaced, and their brightness is anticorrelated. Maksimov and Prosovetsky [2002] have suggested that the brightness anticorrelation is explained by the difference between heights of wave energy release during its transfer from the photosphere to the corona. Increased energy release in lower layers of the magnetic

flux tube leads to an increase in brightness at high frequencies and hence to the appearance of depression higher, in the corona. The situation may also be reverse. Statistical studies have shown that bright sources inside CH at 17 GHz affect characteristics of high-speed solar wind streams [Akiyama et al., 2013].

The purpose of this work is to analyze multiwave CH observations with the Siberian Radioheliograph. We have examined characteristics of microwave structures within the boundaries of the CH observed in EUV emission in the central part of the solar disk on April 25 and September 20, 2023.

OBSERVATIONS

To analyze microwave images, we have used full solar disk maps obtained within a minute at ~06:14 UT on April 25, 2023 during test observations with the Siberian Radioheliograph [Lesovoi et al., 2012; Altyntsev et al., 2020; https://ckp-rf.ru/catalog/usu/4138190/]. Radio maps built automatically in routine mode at 3.0 and 6.2 GHz, and correlation curves in the range 00.00–10.00 UT are available at [https://badary.iszf.irk.ru/srhDaily.php]. The signal accumulation time in these images is 4 s.

Frequencies for antenna arrays 3–6 GHz and 6–12 GHz are listed in the top row of Table. Signals were recorded independently. In each range, observations have been made at 16 frequencies with an accumulation time of 0.2 s at one frequency. A cycle of sequential frequency sampling lasted for less than 4 s. Methods of amplitude and phase calibration in imaging are based on antenna array redundancy and are described in [Globa, Lesovoi, 2021]. Brightness temperatures in the images were calibrated against regions of the quiet Sun. The temperatures of the composite spectrum (we are grateful to A.A. Kochanov for providing the composite spectrum of microwave radiation from the quiet Sun) used in the calibration of the quiet Sun were obtained mainly from measurements made by Zirin et al. [1991] and Borovik et al. [1992] and are presented in the second row of Table.

The low-contrast regions in images with brightness fluctuations were identified by two methods. In the former method, the code developed by M. Globa was used to create radio maps. Coronal holes were studied from the images obtained by averaging radio maps at two adjacent frequencies; in this case, 10 maps, recorded sequentially within a minute, were previously averaged at each frequency. The observation frequencies are listed in the first row of Table. The total signal accumulation time for the dual frequency map is ~4 s. This method was employed to analyze observations of the coronal hole on April 25, 2023. In the latter method, the code developed by S. Anfinogentov was applied to imaging. To increase the accumulation time of a signal from antennas, we first averaged measurements of the visibility of antenna pairs recorded in ten frequency sampling cycles, and then constructed images with an accumulation time of ~3 s at each frequency from them. Figure 1 presents solar disk images for April 25, 2023 (06:14 UT) in EUV (*a*) and microwave (*b*) emissions. A radio map is shown in the frequency range 3.2–3.4 GHz in which the depression region is the closest in shape to the region in the EUV emission. All images are smoothed with a 30″ window and are subjected to equalization of brightness histograms by the IDL procedure hist_equal.pro. The EUV solar disk images were used to determine CH boundaries. We have chosen images in the 193 Å (background and black contours) and 211 Å (yellow contours) lines in which CHs are most pronounced [Garton et al., 2018]. The level of the contours is equal to half of the average brightness over the solar disk. On this day, there are brightness depressions in the polar regions and a large depression region in the center of the solar disk. To identify CHs on the solar disk, we have adopted the procedures CHIMERA [Garton et al., 2018; https://SolarMonitor.org] and SPoCA [https:// suntoday.lmsal.com; Verbeeck et al., 2014]. Note that results of different procedures do not always coincide, especially in determining CH boundaries. The region of equatorial CH obtained with CHIMERA is somewhat narrower than the region of depression in EUV emission and is elongated along red lines in Figure 1.

Figure 2 exhibits CH images (*a*, *c*) at the lowest and highest frequency pairs, presented in Table, together with an EUV image (*b*) and a longitudinal field magnetogram (*d*). The depth of brightness temperature depressions in CHs relative to regions of the quiet Sun decreases with an increase in the receiving frequency. The brightness distributions inside the CH in microwave images are inhomogeneous; there are large-scale meridional ribbons of reduced brightness, narrower at a high frequency. There is a correspondence to some ribbons in the distribution of depression depths in the EUV emission at 211 Å. There is no connection between microwave inhomogeneities and the structure of the longitudinal magnetic field.

To quantify small-scale inhomogeneities of microwave radiation within the equatorial CH, we examine the properties of the brightness temperature histograms in the square inscribed in the CH in Figure 1. For absolute calibration of temperature values, we use the histogram in the square centered at [300, –400] arcsec, located in a quiet Sun region. The maximum of the pixel-by-pixel diagram of this square was assigned the value T_{QS}.

Coronal hole average brightness temperatures as function of frequency

f, GHz	2.8 3.0	3.2 3.4	3.6 3.8	4.0 4.2	4.4 5.0	5.8 6.2	6.6 7.0	7.4 7.8	8.2 8.6	9.0 9.4
T_{QS}, 10^3 K	27.2	23.9	21.5	19.7	17.8	15.1	14.1	13.3	12.7	12.2
T_{mean}, 10^3 K	18.6	16.5	15.2	17.2	14.8	15.3	14.8	14.0	13.0	13.0
T_{mean}/T_{QS}	0.7	0.7	0.7	0.87	0.83	1.01	1.05	1.05	1.02	1.06
T_{min}, 10^3 K	12	11	9	12.5	11	13	12	12	11	11
T_{max}, 10^3 K	30	20	18	21	18	19	17	16	15	14
T_{max}/T_{min}	2.5	1.8	2.0	1.7	1.6	1.5	1.4	1.3	1.4	1.27

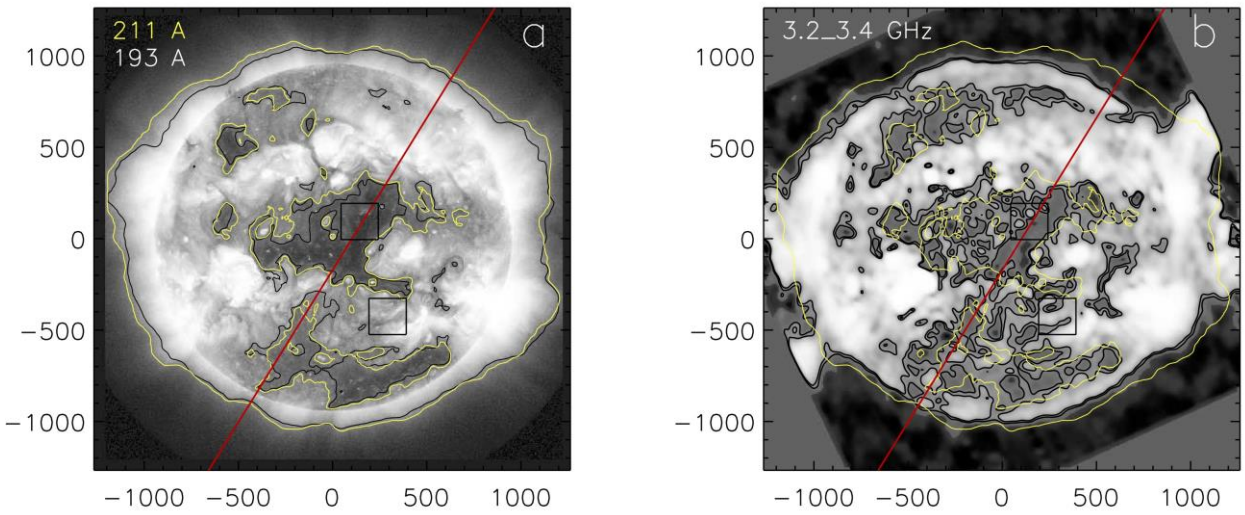

Figure 1. Images of the April 25, 2023 coronal hole. Yellow contours depict regions of depression at half brightness in the 211 Å channel. The images were transformed using the histogram equalization procedure. The background is an SDO/AIA solar disk image in the 211 Å line (*a*). Black contours show brightness depressions in the 193 Å line. A radio map averaged over 3.2 and 3.4 GHz frequencies (*b*). Black contours correspond to the $0.7T_{QS}$ and $0.9T_{QS}$ levels. All images are plotted for 06:14 UT and smoothed with a 30″ window

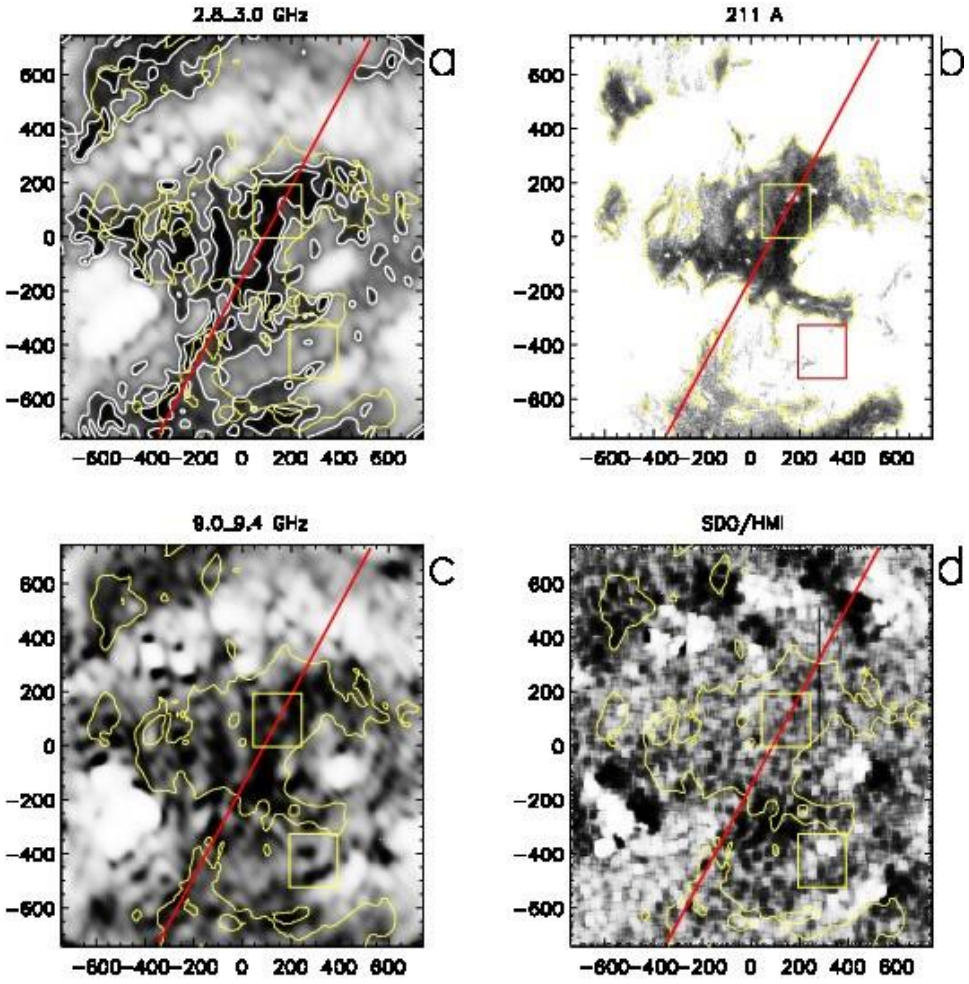

Figure 2. Microwave maps of CH at frequencies with (*a*) and without (*b*) depression. Background images were transformed by equalization and smoothing with a 30″ window. White contours (panel *a*) correspond to $0.7T_{QS}$ and $0.9T_{QS}$. Yellow contours are 0.5 of the mean brightness of the SDO/AIA EUV image in the 211 Å line. Panel *b* is an EUV image in the 211 Å channel. The brightness is cropped from above at 0.6 of the brightness average over the disk to highlight structures inside the CH. Panel *d* presents longitudinal field magnetograms transformed by equalization and smoothing with a window of 30″. Red lines indicate the cross-section for constructing brightness temperature profiles in Figure 3. Squares denote the regions for which the radio brightness histograms were analyzed

Sides of both squares are 200″ with a 4.9″ pixel size. Mean brightness temperatures T_{mean} of CH are presented in Table and are marked with asterisks in Figure 3. Bars show the frequency range along the X-axis and maximum deviations along the Y-axis. At frequencies below 4 GHz, the CH brightness temperature is 1.5 times lower than the temperature of the quiet Sun, then the contrast gradually decreases, and at frequencies above 5–6 GHz the mean brightness of the CH slightly exceeds the temperature of the quiet Sun.

The small-scale distribution of radio brightness over the CH is also inhomogeneous, and the range of the inhomogeneities, i.e. the ratio of maximum to minimum brightness temperatures inside the square, varies from T_{max}/T_{min}=2.5 at the lower end of the frequency range to tens of percent at high frequencies. Note that minimum brightness temperatures T_{min} are as low as 9 TK.

To compare the brightness temperature distributions inside the CH in detail, it is convenient to compare radio brightness profiles at different frequencies. Figure 4, *a*–*c* displays brightness temperature profiles along the cross-section marked in Figure 1, 2 with the red line. Panel *d* depicts the cross-section of EUV emission brightness in the SDO 193 and 211 Å channels, on which boundaries of the depression are indicated by vertical lines. At low frequencies, up to 5.0 GHz, in the region of EUV depression there is a radio emission brightness depression, whereas the temperature profile (*c*) is not gentle as in the EUV emission (*d*), but undergoes variations from $9\cdot10^3$ to $25\cdot10^3$ K.

Significant polarization within the CH boundaries is seen to take place at lower frequencies (Figure 4, *a*, *b*). There are significant fluctuations with an amplitude to 20 % and with a change of sign on the radiation polarization curve at 2.8–3.0 GHz (panel *a*). Fluctuations in panel *b* are much smaller, and they do not correlate with the curve in panel *a*. At high frequencies (see panel *c*), the polarized emission flux is small.

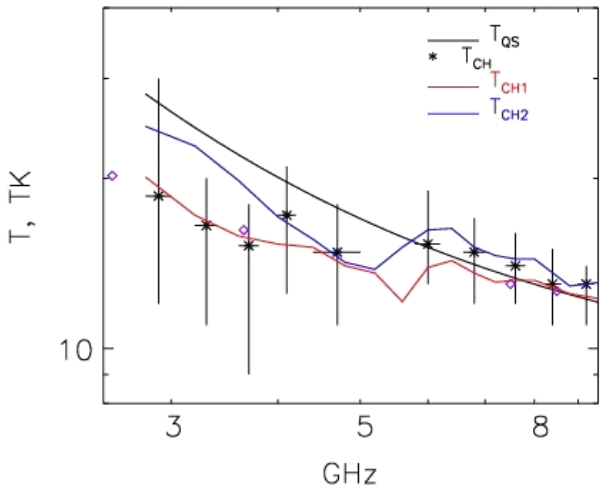

Figure 3. Spectrum of radio emission of the quiet Sun T_{QS} (solid line) and brightness temperatures averaged over CH. Asterisks with bars indicate the spectrum of the April 25, 2023 CH. The bars show T_{max} and T_{min} inside the CH square. Lilac diamonds mark RATAN-600 measurements [Borovik et al., 1990]. Red and blue curves are the CH mean brightness temperatures recorded on September 20, 2023

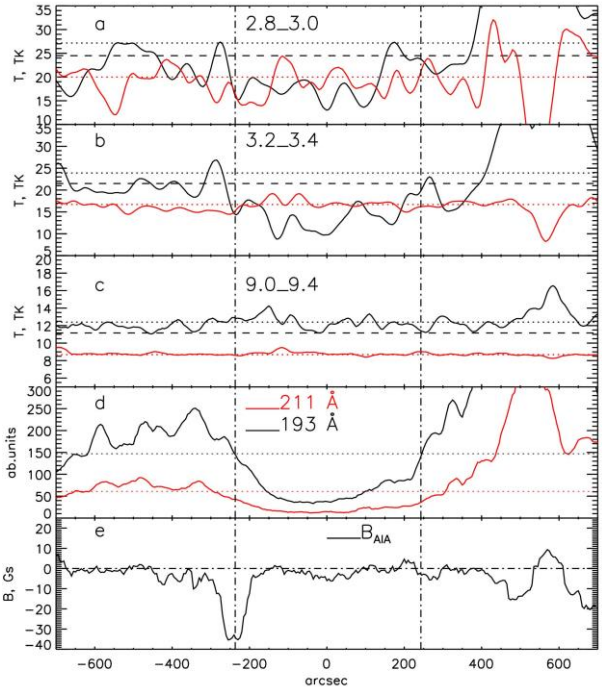

Figure 4. Brightness temperature profiles in intensity (R+L, solid line) (*a*–*c*), plotted along the solar disk cross-sections depicted in Figures 1, 2. Black dotted, dashed, and red dotted lines are the quiet Sun levels $1T_{QS}$, $0.9T_{QS}$, $0.7T_{QS}$. Panel *d* portrays brightness profiles in the 211 and 193 Å lines. Vertical dash-dot lines in all panels are the CH boundaries determined from by the EUV emission in the 193 Å channel; black and red dotted lines correspond to half the brightness in the corresponding channel. All profiles are smoothed by a 30″ window. Panel *e* presents the SDO/HMI magnetogram profile

The cross-section of the magnetogram (Figure 4, *e*) suggests that the magnetic field along the cross-section has a predominantly southerly direction, and its amplitude varies along the cross-section with a scale ~30″, characteristic of chromospheric supergranulation. The line-of-sight photospheric magnetic field component generally does not exceed several Gauss.

Figure 5 presents images for September 20, 2023, constructed by Anfinogentov's method with averaging of visibility functions. The maps and correlation curves obtained in routine mode are available at [https://badary.iszf.irk.ru/srhDaily.php]. For 01:00–01:28 UT, we have obtained images with 1-min increment at 20 frequencies in the range 2.8–11.6 GHz. To increase the signal-to-noise ratio and hence the visibility of depressions at each frequency, they were averaged. The sequence of maps in the 2.8–11.6 GHz range suggests that their changes with frequency is similar to those discussed above for April 25, 2023 maps of the Sun. The depression depth decreases with frequency, and the contrast with the quiet Sun is noticeable at frequencies below 7.2 GHz.

Compare the microwave maps with the distribution of EUV emission over the solar disk at 193 Å and with a magnetogram (Figure 6). The EUV maps exhibit a number of depressions located in the vicinity of the central meridian. There are depressions of two types. The former is associated with coronal holes. The latter corresponds to

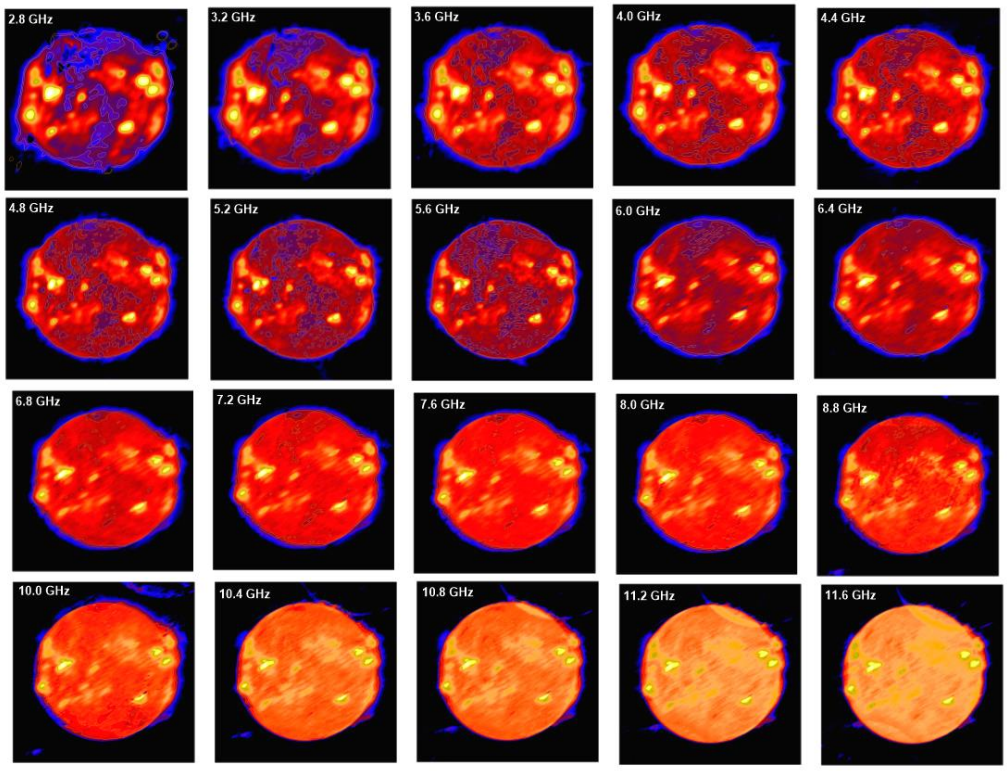

Figure 5. Full solar disk images obtained in the range 2.8–11.6 GHz on September 20, 2023

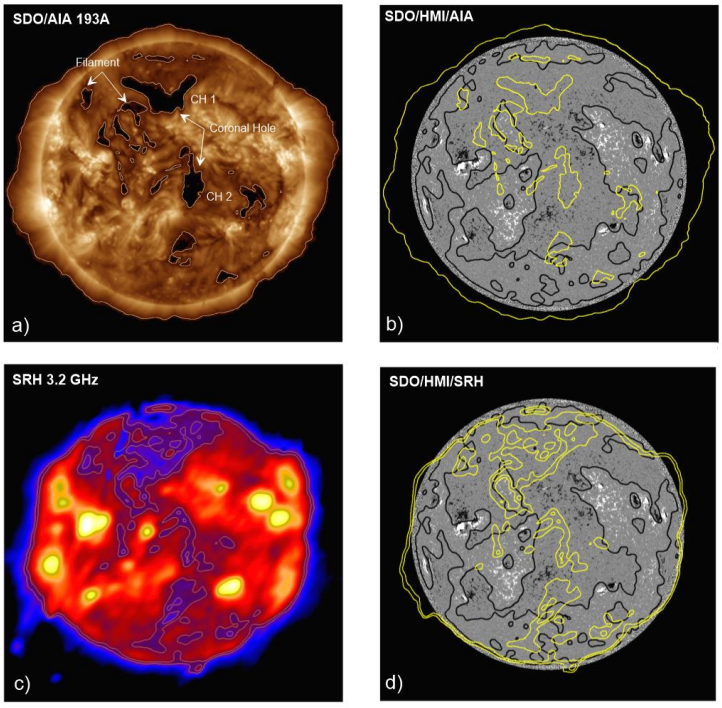

Figure 6. Panel *a* exhibits a solar disk image in the 193 Å EUV channel (*a*), obtained by SDO/AIA on September 20, 2023 (01:00 UT); arrows indicate the identified emission depressions. Panel *b* displays a magnetogram: black contours are the global neutral line of the longitudinal magnetic field; yellow, identified depressions at 193 Å. Panel *c* presents a radio map at 3.2 GHz; contours depict brightness temperature levels $0.7T_{QS}$, $0.9T_{QS}$. Panel *d* shows a magnetogram with superimposed yellow contours of depressions in microwave radiation; black contours are the global neutral line of the longitudinal magnetic field. The depression regions on the microwave map of the solar disk are also elongated approximately along the central meridian. At $0.9T_{QS}$, they are more extensive than regions of half EUV emission brightness, and deep depressions $0.7T_{QS}$ are more compact. The shape of the depression areas generally coincides with the detected depressions in the EUV range. Variations in brightness temperatures in CH with frequency are indicated in Figure 3 by the red curve for the circumpolar hole CH 1 and the blue curve for the equatorial hole CH 2 (*a*). The plots suggest that the frequency dependence of mean brightness temperatures is the same for all coronal holes under study. At low frequencies, the CH brightness is much lower than the level of the quiet Sun and equates to it at receiving frequencies above 6–7 GHz

filaments whose cold matter screens the underlying solar surface. In Figure 6, *a*, the depressions are seen as dark regions with a reduced intensity relative to the average level of the EUV emission of the solar disk. To classify the observed depressions by types, we have used the SDO/AIA magnetogram. Superimposing depression contours on the magnetogram (Figure 6, *b*) shows that structures of different types differ in spatial position relative to the neutral line of a large-scale magnetic field: CH contours cover regions of the longitudinal magnetic field of the same sign, and filaments are located near or along neutral lines of the general solar magnetic field. We can see that at the same time there are regions both along or at an angle to neutral lines (filaments) and completely located in unipolar regions (coronal holes). This criterion of the spatial location of depressions relative to the magnetic field is key in the search for CHs by CHIMERA.

DISCUSSION

SRH radio maps allow us to confidently detect radio brightness depressions associated with CHs. In shape and size, the EUV emission depression regions are the closest to the microwave radiation ones at frequencies ~3–4 GHz. Daily observations with SRH can be used, similarly to extra-atmospheric EUV images, to identify CHs on the solar disk. The contrast of depressions at frequencies around 3 GHz is sufficient to employ machine learning methods similar to that discussed in [Illarionov, Tlatov, 2018].

Test observations with the Siberian Radioheliograph have confirmed the results of CH observations obtained from multiwave one-dimensional scans from RATAN-600 and two-dimensional maps from SSRT (5.7 GHz) and the Nobeyama Radioheliograph (17 GHz).

In Figure 3, lilac diamonds mark the results of RATAN-600 measurements of the radio spectrum averaged for 4 CHs obtained during minimum solar activity in 1984–1986 [Borovik et al., 1990]. According to [Borovik et al., 1990], the frequency above which the contrast between CH brightness temperatures and the quiet Sun disappears is 7.5 GHz. Note that the depressions recorded by RATAN-600 and SRH are close in depth. For the polar CH observed during the March 29, 2006 solar eclipse, Golubchina [2022] has estimated the frequency above which brightness temperatures of CH and the quiet Sun reach the same level at 5 GHz.

Dravskikh and Dravskikh [2023] discuss RATAN-600 measurements of CH spectra. In this work, based on observations of 22 CHs during the descending phase of solar cycle 24, the average frequency of contrast disappearance is taken to be 10 GHz. Unfortunately, the paper does not discuss the accuracy of CH emission identification on one-dimensional scans of the active Sun's disk. The advantage of SRH two-dimensional observations is the ability to identify CHs during high solar activity when there are many active regions on the solar disk. For three CHs recorded during SRH test observations, the average frequency of contrast disappearance is in the vicinity of 6 GHz (see Figure 3).

It follows from Figure 2 that the structures of reduced brightness with scales >100″ can be traced in the microwave range from 2.8 to 10 GHz. These structures do not clearly correlate with the distribution of the longitudinal magnetic field component. There are almost no inhomogeneities in EUV emission (see Figure 4). Pixel-to-pixel analysis of the brightness temperature in CH also shows the presence of small-scale (several arcsec) inhomogeneities. The pixel-to-pixel brightness at a frequency of 2.8 GHz reaches T_{max}/T_{min}=2.5, and with increasing frequency it decreases to 1.3 at ~10 GHz.

The microwave radiation of the quiet Sun and CHs is generated by the bremsstrahlung mechanism and consists, in the first approximation, of radiation from two layers: the optically thick chromosphere and the optically thin corona in the height range to 40 thousand km [Bogod, Grebinckij, 1997]. Depressions manifest themselves at low frequencies, at which the contribution of the coronal layer is large, and are attributed to ~1.5 time lower plasma density and temperature in the corona above CH relative to the quiet Sun [Borovik et al., 1999].

It is interesting to discuss the unique results obtained by Borovik et al. [1999] on estimate of the magnetic field in the corona over CH. The high sensitivity of RATAN-600 made it possible to measure the degree of polarization at ~3 GHz — 0.2 %. In the case of the bremsstrahlung mechanism, we can calculate the magnetic field component along the line of sight [Gelfreikh, 2004]:

$$B = 107\frac{P}{n\lambda},$$

where B is the magnetic field [G]; P is the degree of polarization [%]; n is the power law factor of the microwave spectrum; λ is the emission wavelength [cm]. The value $n \approx 0.9$ is determined from the CH emission spectrum. Thus, for 3 GHz, the magnetic field along the line of sight is 2–3 G.

The April 25, 2023 event exhibits fluctuations in the degree of polarization within the CH with an amplitude to 20 % (see Figure 4). The average degree of polarization in the CH is also significant: from 3.7 % at 2.8–3.0 GHz to 0.95 % at 3.2–3.4 GHz. Accordingly, the averaged estimates of the magnetic field for these frequencies are unexpectedly high — 16.8 and 4.9 G. A close estimate of the degree of polarization $P \approx 1.5$ % was obtained at a low frequency for CH2 on September 20, 2024. Yet, in this case in the small-scale CH, polarization does not disappear with increasing frequency, but increases on average. We can conclude that in the test observations under discussion a high level of noise fluctuations and, possibly, traces of side lobes did not allow us to achieve the minimum level of measurements of the degree of polarization with RATAN-600. Solving this problem requires observations of a large-scale CH with a low level of side lobes and a signal accumulation time of several minutes.

CONCLUSION

Test observations of coronal holes with two antenna arrays in 3–6 and 6–12 GHz ranges have shown the high diagnostic potential of the Siberian Radioheliograph.

Spectral observations with SRH will provide unique information about the dynamics and structure of the solar atmosphere over CHs from the chromosphere to the lower corona, as well as about the physical nature of inhomogeneities inside CHs, including features of magnetic field distribution.

The use of regular mapping of the solar disk in applied problems of forecasting solar wind variations is promising. SRH observations can provide the main CH parameters employed in forecasting (location and shape of depression regions, depth of depression, flare activity at CH boundaries, brightness inhomogeneities in CHs), which are currently obtained from extra-atmospheric observations of EUV emission.

We are grateful to the team of the ISTP SB RAS Radioastrophysical Observatory for providing SRH data.

The work was financially supported by RSF (Grant No. 22-22-00019). The study was carried out with the financial support from the Ministry of Science and Higher Education of the Russian Federation with budgetary funding of Program II.16.3.2 "Nonstationary and Wave Processes in the Solar Atmosphere". The results were obtained using the equipment of Shared Equipment Center «Angara» [http://ckp-rf.ru/ckp/3056].

REFERENCES

Akiyama S., Gopalswamy N., Yashiro S., Mäkelä P. A study of coronal holes observed by SOHO/EIT and the Nobeyama Radioheliograph. *Publications of the Astronomical Society of Japan*. 2013, vol. 65, S15. DOI: 10.1093/pasj/65.sp1.S15.

Altyntsev A.T., Lesovoi S.V., Globa M.V., Gubin A.V., Kochanov A.A., Grechnev V.V., Ivanov E.F., et al. Multiwave Siberian Radioheliograph. *Solar-Terr. Phys.* 2020, vol. 6, iss. 2, pp. 30–40. DOI: 10.12737/stp-62202003.

Bogod V.M., Grebinskij A.S. Large-scale structure of the atmosphere of the quiet sun, coronal holes, and plages as deduced by tomography study. *Solar Phys.* 1997, vol. 176, iss. 1, pp. 67–86. DOI: 10.1023/A:1004929418335.

Borovik V.N., Kurbanov M.S., Livshits M.A., Ryabov B.I. Coronal holes against the background of the quiet Sun — observations with the RATAN-600 in the 2–32-cm range. *Soviet Astronomy*. 1990, vol. 34, no. 5, p. 522.

Borovik V.N., Kurbanov M.S., Makarov V.V. Distribution of radio brightness of the quiet Sun in the 2–32-cm range. *Soviet Astronomy*. 1992, vol. 36, no. 6/NOV, p. 656.

Borovik V.N., Medar V.G., Korzhavin A.N. First measurements of the magnetic field in a coronal hole from RATAN-600 radio observations of the Sun. *Astron. Lett.* 1999, vol. 25, iss. 4, pp. 250–257.

Cranmer S.R. Coronal Holes. *Living Reviews in Solar Physics.* 2009, vol. 6, iss. 1, 3, 66 p. DOI: 10.12942/lrsp-2009-3.

Dravskikh A.F., Dravskikh Yu.A. Adiabatic radio emission spectrum of the Sun's coronal holes. *Astron. Rep.* 2023, vol. 67, pp. 513–519. DOI: 10.1134/S1063772923050037.

Garton T.M., Gallagher P.T., Murray S.A. Expansion of high-speed solar wind streams from coronal holes through the inner heliosphere. *Journal of Space Weather and Space Climate*. 2018, vol. 8, id. A02, 12 p. DOI: 10.1051/swsc/2017039.

Gelfreikh G.B. Coronal magnetic field measurements through bremsstrahlung emission. *Solar and Space Weather Radiophysics*. 2004, p. 115. DOI: 10.1007/1-4020-2814-8_6.

Globa M.A., Lesovoi S.V. Calibration of Siberian Radioheliograph antenna gains using redundancy. *Solar-Terr. Phys.* 2021, vol. 7, iss. 4, pp. 98–103. DOI: 10.12737/stp-74202111.

Golubchina O.A. Investigation of the polar coronal hole in the Sun with RATAN-600 in the centimeter radio range. *POS. Vol. 425: The Multifaceted Universe: Theory and Observations – 2022 (MUTO2022).* 2022, 063. URL: https://pos.sissa.it/425/063/pdf (accessed 19.06.2024).

Gopalswamy N., Shibasaki K., Thompson B.J., Gurman J., DeForest C. Microwave enhancement and variability in the elephant's trunk coronal hole: Comparison with SOHO observations. *J. Geophys. Res*. 1999, vol. 104, pp. 9767–9780. DOI: 10.1029/1998JA900168.

Grechnev V.V., Lesovoi S.V., Smolkov G.Ya., Krissinel B.B., Zandanov V.G., Altyntsev A.T., et al. The Siberian Solar Radio Telescope: the current state of the instrument, observations, and data. *Solar Phys*. 2003, vol. 216, pp. 239–272. DOI: 10.1023/A:1026153410061.

Illarionov E.A., Tlatov A.G. Segmentation of coronal holes in solar disc images with a convolutional neural network. *Monthly Notices of the Royal Astronomical Society*. 2018, vol. 481, iss. 4, pp. 5014–5021. DOI: 10.1093/mnras/sty2628.

Kosugi T., Ishiguro M., Shibasaki K. Polar-cap and coronal-hole-associated brightenings of the Sun at millimeter wavelengths. *Publications of the Astronomical Society of Japan*. 1986, vol. 38, pp. 1–11.

Krieger A.S., Timothy A.F., Roelof E.C. A coronal hole and its identification as the source of a high velocity solar wind stream. *Solar Phys.* 1973, vol. 29, pp. 505–525. DOI: 10.1007/BF00150828.

Krissinel B.B., Kuznetsova S.M., Maksimov V.P., Prosovetsky D.V., Grechnev V.V., Stepanov A.P., Shishko L.F.Some features of manifestations of coronal holes in microwave emission. 2000. *Publications of the Astronomical Society of Japan*. 2000, vol. 52, iss. 5, pp. 909–917. DOI: 10.1093/pasj/ 52.5.909.

Lesovoi S.V., Altyntsev A.T., Ivanov E.F., Gubin A.V. The Multifrequency Siberian Radioheliograph. *Solar Phys.* 2012, vol. 280, pp. 651–661. DOI: 10.1007/s11207-012-0008-7.

Maksimov V.P., Prosovetsky D.V. Coronal heating in the coronal holes regions. *Solar Variability: From Core to outer Frontiers. The 10th European Solar Physics Meeting, 9–14 September 2002, Prague, Czech Republic*. ESA SP-506, Vol. 2. Noordwijk: ESA Publications Division, 2002, pp. 689–692.

Maksimov V.P., Prosovetsky D.V., Grechnev V.V., Krissinel B.B., Shibasaki K. On the relation of brightness temperatures in coronal holes at 5.7 and 17 GHz. *Publications of the Astronomical Society of Japan*. 2006, vol. 58, pp. 1–10. DOI: 10.1093/pasj/58.1.1.

Moran T., Gopalswamy N, Dammasch I.E., Wilhelm K. A multi-wavelength study of solar coronal-hole regions showing radio enhancements. *Astron. and Astrophys*. 2001, vol. 378, pp. 1037–1045. DOI: 10.1051/0004-6361:20010569.

Nakajima H., Nishio M., Enome S., Shibasaki K., Takano T., Hanaoka Y., Torii C., et al. The Nobeyama Radioheliograph. *Proc. IEEE*. 1994, vol. 82, pp. 705–713.

Nolte J.T., Krieger A.S., Timothy A.F., Gold R.E., Roelof E.C., Vaiana G., Lazarus A.J., Sullivan J.D., McIntosh P.S. Coronal holes as sources of solar wind. *Solar Phys*. 1976, vol. 46, pp. 303–322. DOI: 10.1007/BF00149859.

Obridko V.N., Shelting B.D., Livshits I.M., Asgarov A.B. Contrast of Coronal Holes and Parameters of Associated Solar Wind Streams. *Solar Phys*. 2009, vol. 260, pp. 191–206. DOI: 10.1007/s11207-009-9435-5.

Papagiannis M.D., Baker K.B. Determination and Analysis of Coronal Hole Radio Spectra. *Solar Phys.* 1982, vol. 79, pp. 365–374. DOI: 10.1007/BF00146252.

Pohjolainen S., Portier-Fozzani F., Ragaigne D. Comparison of 87 GHz solar polar structures with EUV and soft X-ray emission. *American Astronomical Society*. 2000, vol. 143, pp. 227–263. DOI: 10.1051/aas:2000179.

Reiss M.A., Temmer M., Veronig A.M., Nikolic L., Vennerstrom S., Schöngassner F., Hofmeister S.J. Verification of high-speed solar wind stream forecasts using operational solar wind models. *Space Weather*. 2016, vol. 14, pp. 495–511. DOI: 10.1002/2016SW001390.

Rotter T., Veronig A.M., Temmer M., Vršnak B. Relation between coronal hole areas on the sun and the solar wind parameters at 1 AU. *Solar Phys.* 2012, vol. 281, pp. 793–813. DOI: 10.1007/s11207-012-0101-y.

Rotter T., Veronig A.M., Temmer M., Vršnak B. Real-time solar wind prediction based on SDO/AIA coronal hole data. *Solar Phys.* 2015, vol. 290, pp. 1355–1370. DOI: 10.1007/s11207-015-0680-5.

Verbeeck C., Delouille V., Mampaey B., De Visscher R. The SPoCA-suite: Software for extraction, characterization, and tracking of active regions and coronal holes on EUV images. *Astron. Astrophys*. 2014, vol.561, id. A29, 16 p. DOI: 10.1051/ 0004-6361/201321243.

Vršnak B., Temmer M., Veronig A.M. Coronal holes and solar wind high-speed streams: I. Forecasting the solar wind parameters.*Solar Phys*. 2007, vol. 240, pp. 315–330. DOI: 10.1007/s11207-007-0285-8.

Zirin H., Baumert B.M., Hurford G.J. The microwave brightness temperature spectrum of the quiet Sun. *Astrophys. J*. 1991, vol. 370, p. 779. DOI: 10.1086/169861.

Wang Y.-M., Sheeley N.R., Jr. Solar wind speed and coronal flux-tube expansion. *Astrophys. J*. 1990, vol. 355, p. 726. DOI: 10.1086/168805.

URL: https://badary.iszf.irk.ru/srhDaily.php (accessed May 19, 2024).

URL: https://SolarMonitor.org (accessed May 19, 2024).

URL: https://suntoday.lmsal.com (accessed May 19, 2024).

URL: http://ckp-rf.ru/ckp/3056/ (accessed May 19, 2024).

URL: https://ckp-rf.ru/catalog/usu/4138190/ (accessed May 19, 2024).

This paper is based on material presented at the 19th Annual Conference on Plasma Physics in the Solar System, February 5–9, 2024, IKI RAS, Moscow.

Original Russian version: Altyntsev A.T., Globa M.V., Meshalkina N.S., Sych R.A., published in Solnechno-zemnaya fizika. 2024. Vol. 10. No. 3. P. 5–12. DOI: 10.12737/szf-103202401.

How to cite this article

Altyntsev A.T., Globa M.V., Meshalkina N.S., Sych R.A. Observations of coronal holes with the Siberian Radioheliograph. *Solar-Terrestrial Physics*. 2024. Vol. 10, Iss. 3. P. 3–10. DOI: 10.12737/stp-103202401.